Supporting Information

The Role of Gold Nanoparticles' Aspect Ratio in Plasmon-Enhanced Luminescence and Singlet Oxygen Generation Rate by Mo_6 Clusters

*Evgeniya D. Novikova,[a] Yuri A. Vorotnikov,[*a] Nazar A. Nikolaev,[b] Alphiya R. Tsygankova,[a] Michael A. Shestopalov[a], Olga A. Efremova,[*c]*

[a]Nikolaev Institute of Inorganic Chemistry SB RAS, 3 Acad. Lavrentiev ave., 630090 Novosibirsk, Russian Federation.
[b]Institute of Automation and Electrometry SB RAS, 1, Acad. Koptyuga ave., 630090 Novosibirsk, Russian Federation.
[c]Scientific Institute of Clinical and Experimental Lymphology – branch of ICG SB RAS, 2 Timakova str., 630060 Novosibirsk, Russian Federation.

*Corresponding Authors:
*Yuri A. Vorotnikov
Tel. +7-383-330-92-53, Fax +7-383-330-94-89
e-mail: vorotnikov@niic.nsc.ru
[*]Olga A. Efremova
Tel.: +44 7583012446.
e-mail: olgaa.efremova@gmail.com

Content

Experimental part

Materials

$(Bu_4N)_2[\{Mo_6I_8\}L_6]$ (L = NO_3^- (**1**) or OTs^- (**2**)) were synthesised according to previously reported procedures.[1, 2] All other reactants and solvents were purchased from Fisher, Alfa Aesar and Sigma-Aldrich and were used as received.

Methods

The gold and molybdenum content in all samples was determined on a high-resolution spectrometer iCAP-6500 (Thermo Scientific) with a cyclone-type spray chamber and a «SeaSpray» nebulizer. Prior to the elemental analysis, the samples were boiled in a mixture of HNO_3 and HCl (1:3, v/v) on a water bath. The spectra were obtained by axial plasma viewing. The standard operating conditions of the ICP-AES system were: power – 1150 W, inner diameter of injector – 3 mm, carrier argon flow – 0.7 L min^{-1}, accessorial argon flow – 0.5 L min^{-1}, cooling argon flow – 12 L min^{-1}, number of parallel measurements – 3, integration time – 5 s. Deionised water (R ≈ 18 MΩ) was used to prepare the sample solutions. All the chemical reagents were of analytical grade.

UV-vis absorption spectra of particle dispersions were recorded at room temperature on a Cary 60 UV-Vis Spectrophotometer (Agilent). The fluorescence emission spectra were obtained for the particle dispersions on a Cary Eclipse (Agilent) at λ_{ex} = 365 nm. Prior to the measurements, we determined the molybdenum content using ICP-AES. Further, the dispersions of the particles were diluted to get similar concentrations of Mo = 36 μg_{Mo} mL^{-1}. The particle size and morphology were characterised by transmission electron microscopy (TEM) with a Libra 120 (Zeiss, Germany) at an acceleration voltage of 60 kV and by Dynamic light scattering (DLS) with Photocor Compact-Z equipment (Russia).

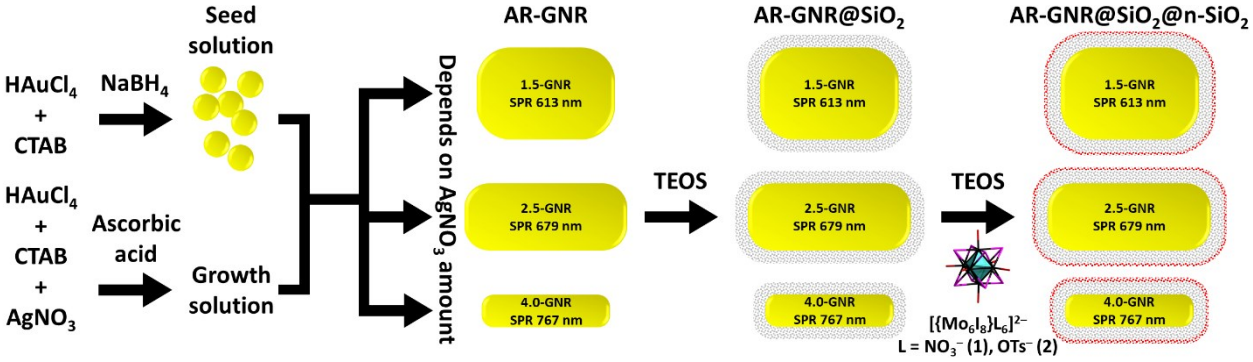

Figure S1. The synthetic procedure of AR-GNR@SiO_2@**n**-SiO_2.

Synthesis of gold nanorods with different aspect ratios (AR-GNRs)

Gold nanorods were synthesised by the seed-mediated growth method described by Nikoobakht and El-Sayed.[3] Firstly, 250 µL of 0.01 M $HAuCl_4$ was added to 10 mL of cetyltrimethylammonium bromide (CTAB) solution (0.1 M). Then, 800 µL of ice-cold $NaBH_4$ (0.01 M) was injected into the mixture and vigorously stirred for 2 min. The colour of the solution changed from bright yellow to brown indicating the formation of Au seeds. The seed solution was used after 2 hours of incubation at room temperature.

The growth solution was prepared in the following manner. 2 mL of $HAuCl_4$ (0.01 M), 300, 500 or 800 µL of $AgNO_3$ (0.01 M), 800 µL of HCl (1 M) and 320 µL of ascorbic acid (0.1 M) were successively added to 40 ml of CTAB (0.1 M) solution. After the addition of ascorbic acid, the solution became colourless. Then, 96 µL of seed solution was immediately injected to the mixture under gentle stirring for 30 s. The resulted solution was kept undisturbed overnight.

PSS-stabilisation of AR-GNRs

Prior to coating, AR-GNRs were stabilised with sodium polystyrene sulfonate (PSS) to avoid particle aggregation.[4] CTAB-stabilised GNRs solution was centrifuged (16000 rpm, 10 min, twice) in order to remove excess of CTAB and then diluted in water to give final volume of 20 mL. Then, the aqueous solution of GNRs was mixed with chloroform (10 mL) and shaken for 30 s to produce an emulsion. The phases were separated by centrifugation (3000 rpm, 4 min, twice). The aqueous phase was removed, treated with a 30 mL 1% w/v PSS solution and stirred for 1 h. Then the solution was centrifuged (16000 rpm, 10 min, twice) and re-dispersed in 2 mL of pure water.

Synthesis of AR-GNR@SiO_2@$\mathbf{n}^{1.5}$-SiO_2 with different silica shell thicknesses

Silica coated GNRs were synthesised via the modified Stöber sol-gel method. Prior to coating, 2 mL of PSS-stabilised GNRs were mixed with 14 mL of ethanol and 200 µL of concentrated aqueous ammonia solution. Each specific volume of TEOS/ethanol solution (1:4 v/v) (specified in Table S1) was injected to nanoparticle dispersion to form the inner silica shell. After stirring for 24 h, 10 µL of TEOS/ethanol (1:4 v/v) and 800 µL of **1** in acetone (1 mg mL^{-1}) were added to the reaction mixture and stirred for another 24 h. The resultant colloid solution was washed with acetone and water for several times and re-dispersed in 4 mL of pure water.

Table S1. Volume of TEOS/ethanol solution added into the reaction

GNRs sample	TEOS/ethanol (1:4 v/v), µL
1.5-GNRs	15
	30
	50
2.5-GNRs	25
	50
	75
4.0-GNRs	50
	100
	150

Synthesis of AR-GNR@SiO_2@$\mathbf{n}^{x}$-SiO_2 with varied content of 1 and AR-GNR@SiO_2@$\mathbf{2}^{3}$-SiO_2

AR-GNR@SiO_2@$\mathbf{n}^{x}$-SiO_2, where x = 1.5, 2.3 and 3 mg per 1 mg of SiO_2 in the case of **1** and 3 mg per 1 mg of SiO_2 in the case of **2**, were synthesised as described above. In order to form the inner silica shell, 30, 50 or 100 µL of TEOS/ethanol solution was used for 1.5-GNRs, 2.5-GNRs or 4.0-GNRs, respectively. The outer silica shell was formed by addition of 10 µL of TEOS/ethanol (1:4 v/v) and 0.8, 1.2 or 1.6 mL of **1** in acetone (1 mg/mL) in the case of AR-GNR@SiO_2@$\mathbf{1}^{x}$-SiO_2 or 1.6 mL of **2** in acetone (1 mg/mL) in the case of AR-GNR@SiO_2@$\mathbf{2}^{3}$-SiO_2.

Synthesis of GNP@SiO_2@$\mathbf{n}^{3}$-SiO_2

Gold nanoparticles (GNPs) were synthesised with a size of 88±6 nm and their coating with cluster-containing silica (25±1 nm) (according to TEM, Figure S2) were performed by the method described in [5].

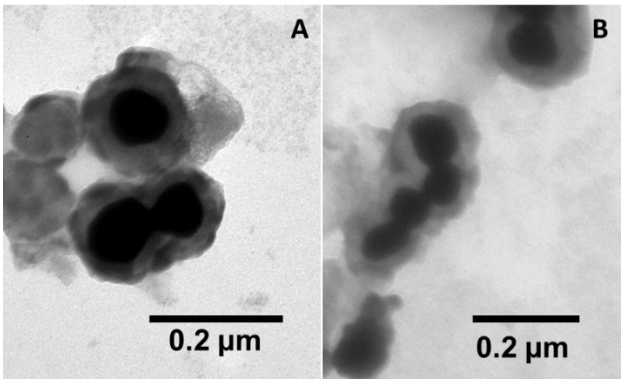

Figure S2. TEM image of GNP@SiO_2@**n**^{3}-SiO_2, n = **1** (A) and **2** (B).

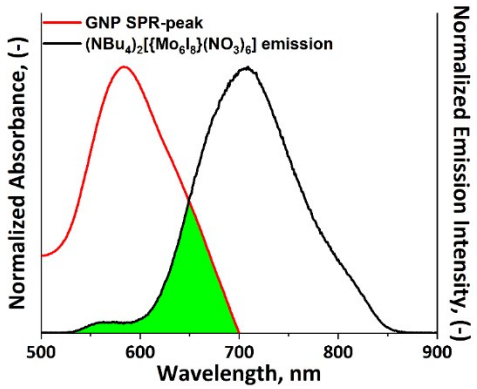

Figure S3. Overlapping (green area) of SPR peaks of GNP (red line) and emission spectra of $(Bu_4N)_2[\{Mo_6I_8\}(NO_3)_6]$ (black line), λ_{ex} = 365 nm.

Singlet oxygen ($^1O_2$) generation

1,5-dihydroxynaphtalene (DHN), a well-known singlet oxygen trap, was used to determine singlet oxygen ($^1O_2$) generation efficiency. Prior to the photochemical experiment, we determined the molybdenum content in the as-prepared particles using ICP-AES. Further, the dispersions of particles were diluted to get similar concentrations of Mo (36 μg_{Mo} mL^{-1}) and added to 30 mL of DHN solution in acetonitrile ($2x10^{-4}$ M). The resultant colloid was stirred for 5 min. The mixtures were irradiated using a Hamamatsu Photonics LED head unit L11921-400 (wavelength 365±5 nm) used with a LED controller C11924-211 (670 mW). At regular intervals of irradiation time (0, 2, 4, 6, 8, 10, 12 min), 3 mL aliquots were collected. All aliquots were centrifuged and UV-vis spectra of the supernatants were recorded. To determine $^1O_2$ generation efficiency absorption at 298 nm vs irradiation time was plotted and analysed as a reaction that follows first order kinetics.

Measurement of photothermal activity

3 mL of aqueous solutions of 4.0-GNR@SiO_2 or 4.0-GNR@SiO_2@**n**-SiO_2 (utilised concentration of $3.2 \cdot 10^{10}$ particles mL^{-1} was calculated using ISP-AES data (C_{Au} = 4.8 µM), crystalline gold density (19.3 g cm^{-3}), and dimensional characteristics of the particles) were placed into an open quartz ampoule and then irradiated using Ti:sapphire laser pulses (MULTUS MPAPOP-1000K, Avesta Ltd., Russia). A fundamental harmonic with a wavelength of about 800 nm was used in the study. The pulse width, repetition rate, and power delivered to the sample were 60 fs, 1 kHz, and 600 mW respectively. The temperature of the sample was controlled by an ANSI Type K (chromel-alumel) thermocouple connected to the calibrated temperature controller (Termodat-13E1, Control Systems Co. Ltd., Russia) placed outside of the laser beam. The temperature difference from the initial sample temperature, ΔT, was recorded at regular intervals.

Optimisation of the silica shell thickness

The silica shell thickness that provides the maximal plasmonic enhancement of luminescent and photodynamic properties was determined in a similar manner to previously described work.[5] 1.5 mg of was used to dope 1 g of SiO_2. The shell thickness was tuned by varying the amount of TEOS used in the reaction mixture (Table S1). The dimensional characteristics of the obtained materials as well as the resulting shell thickness were determined from TEM images (Figure S4-S6) are summarised in Tables S2 and S3. The absorption spectra of the aqueous colloid solution of the obtained nanoparticles showed a consistent bathochromic shift of the SPR maxima with the growth of silica shell thickness (Figure S7). The increase of SPR is due to the fact that the dielectric constant of silica is larger than that of water.[6]

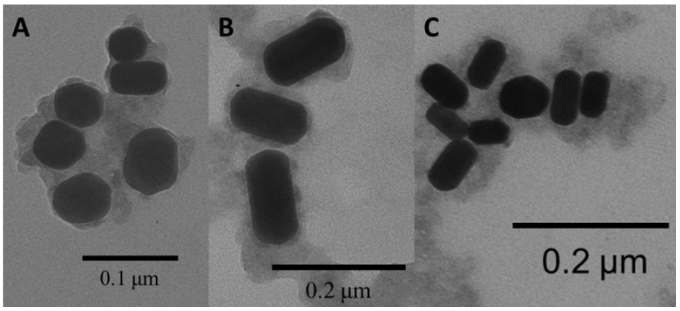

Figure S4. TEM image of 1.5-GNR@SiO_2@**1**$^{1.5}$-SiO_2 with different shell thickness: 5 ± 1 nm (A), 7 ± 1 nm (B), and 20 ± 4 nm (C).

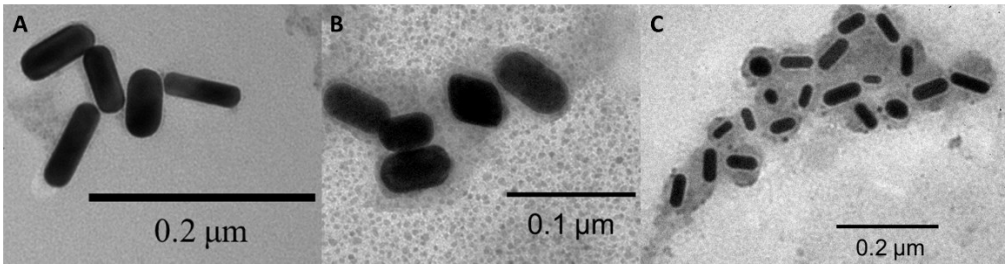

Figure S5. TEM image of 2.5-GNR@SiO_2@**1**$^{1.5}$-SiO_2 with different shell thickness: 5 ± 1 nm (A), 8 ± 1 nm (B), and 19 ± 2 nm (C).

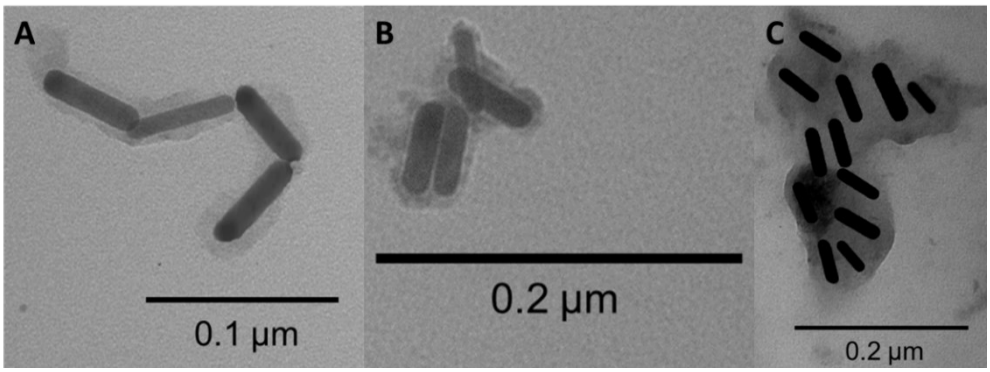

Figure S6. TEM image of 4.0-GNR@SiO_2@**1**$^{1.5}$-SiO_2 with different shell thickness: 6 ± 1 nm (A), 10 ± 1 nm (B), and 17 ± 2 nm (C).

Table S2. SPR peak maxima determined using UV-vis and dimensional characteristics resolved using TEM of GNP and AR-GNR.

Sample	SPR peak maximum, nm	GNR length, nm	GNR width, nm	GNR aspect ratio (AR)
GNP	584	88 ± 6	88 ± 6	1
1.5-GNRs	613	56 ± 5	37 ± 6	1.5
2.5-GNRs	679	66 ± 5	27 ± 3	2.5
4.0-GNRs	767	52 ± 3	13 ± 1	4.0

Table S3. Silica shell thickness in AR-GNR@SiO_2@$n^{1.5}$-SiO_2.

Sample	Silica shell thickness, nm
1.5-GNRs	5 ± 1
	7 ± 1
	20 ± 4
2.5-GNRs	5 ± 1
	8 ±1
	19 ± 2
4.0-GNRs	6 ± 1
	10 ± 1
	17 ± 2

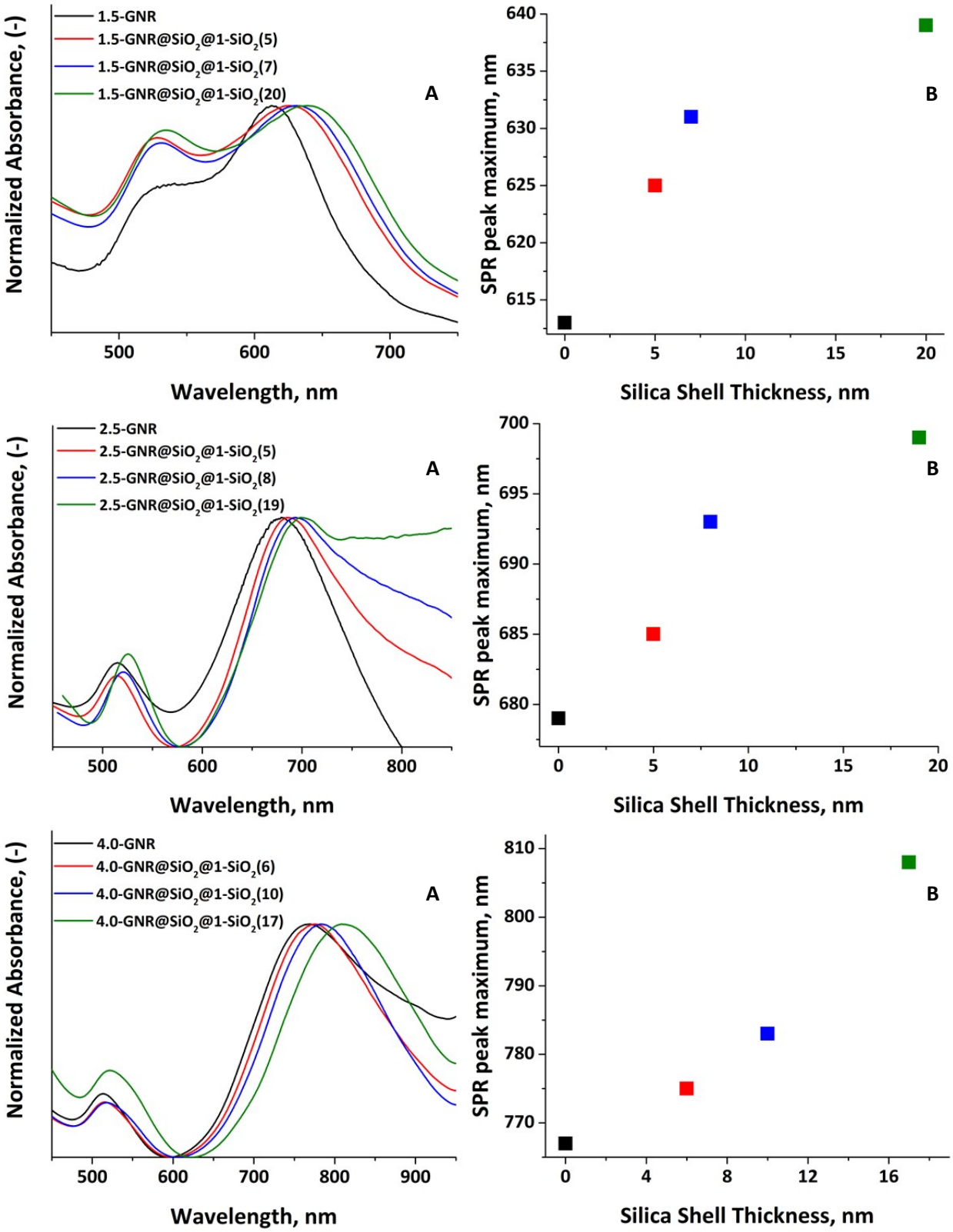

Figure S7. UV-vis spectra of AR-GNR@SiO_2@**1**$^{1.5}$-SiO_2 with different shell thickness (A) and SPR peak position of AR-GNR@SiO_2@**1**$^{1.5}$-SiO_2 vs silica shell thickness (B).

The impact of cluster-to-gold core distances on the luminescent properties of materials was demonstrated by recording the emission spectra for the samples with different shell thickness (Figure S8). All samples have shown a broad emission band typical for clusters and cluster-containing materials with maxima highly dependent on the AR of the GNR used. The luminescence intensity was also greatly dependent on the silica shell thickness. For the samples with shell thickness of 5-6 and 17-20 nm, the intensities at the emission maximum were almost similar. On the other hand, a noticeable increase in emission intensity was observed when the silica shell thickness was 7-10 nm. Therefore, the particles with the highest emission intensities were used further to determine the optimal cluster content.

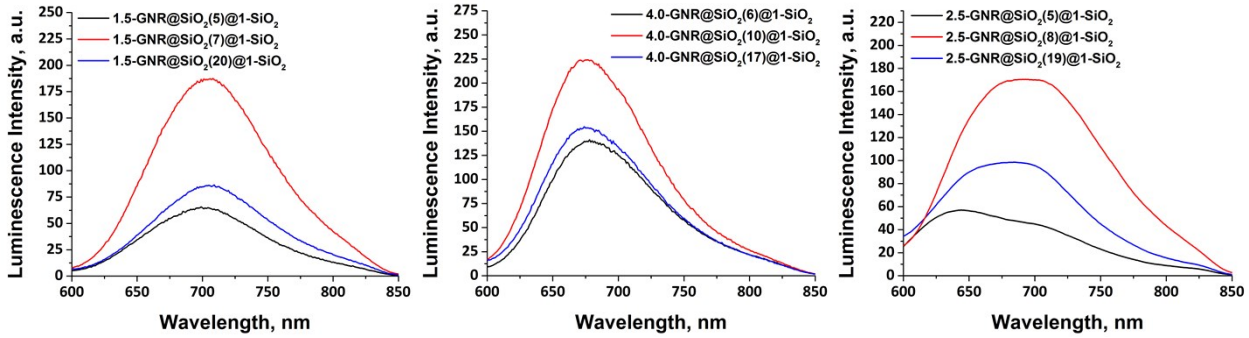

Figure S8. Emission spectra of AR-GNR@SiO_2@**1**$^{1.5}$-SiO_2 with different shell thickness. λ_{ex} = 365 nm.

Optimisation of the cluster content in the material

To define the optimal amount of the included cluster complex, silica coated GNR were synthesised in the presence of **1**, AR-GNR@SiO_2@**1**^{x}-SiO_2, where x is the content of **1** equal to 1.5, 2.3 or 3 mg per 1 mg of SiO_2. The emission spectra of the aqueous dispersion of the nanoparticles demonstrated an overall tendency of luminescence intensity to increase with the increase of the cluster loading with maxima at x = 3 in all cases (Figure S9).

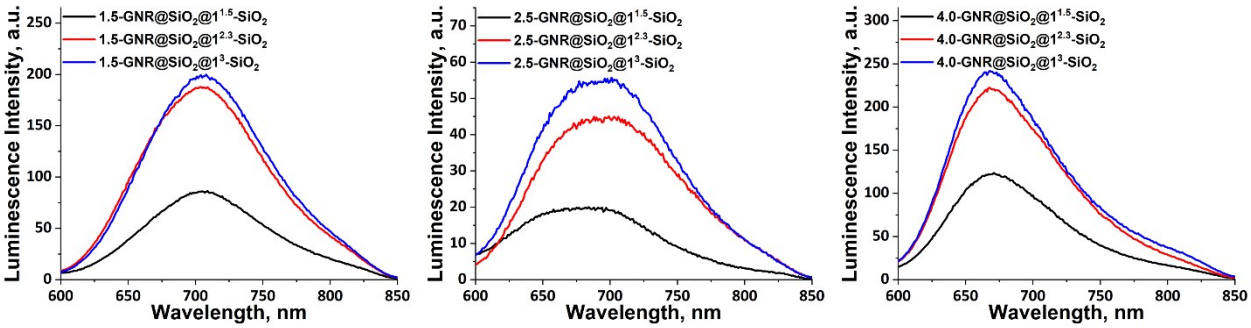

Figure S9. Emission spectra of AR-GNR@SiO_2@**1**^{x}-SiO_2 particles with different cluster content. λ_{ex} = 365 nm.

DLS measurements of GNP@SiO_2@2-SiO_2 and AR-GNR@SiO_2@1^3-SiO_2

Table S4. DLS data on GNP@SiO_2@**1**-SiO_2 and AR-GNR@SiO_2@**1**-SiO_2 with different AR.

Sample	Hydrodynamic Radius, nm	PDI
GNP@SiO_2@**1**-SiO_2	42.6	0.03
1.5-GNR@SiO_2(5)@**1**-SiO_2	25.8	0.05
1.5-GNR@SiO_2(7)@**1**-SiO_2	29.6	0.05
1.5-GNR@SiO_2(20)@**1**-SiO_2	33.5	0.04
2.5-GNR@SiO_2(5)@**1**-SiO_2	18.5	0.06
2.5-GNR@SiO_2(8)@**1**-SiO_2	28.4	0.06
2.5-GNR@SiO_2(19)@**1**-SiO_2	30.2	0.09

4.0-GNR@SiO_2(6)@**1**-SiO_2	34.7	0.1
4.0-GNR@SiO_2(10)@**1**-SiO_2	35.0	0.1
4.0-GNR@SiO_2(17)@**1**-SiO_2	22.3	0.1

Proposed mechanism of emission intensity and singlet oxygen production enhancement

Luminescence process in the absence of plasmonic unit is well described by Jablonski diagram (Figure S10) and quantified by excitation efficiency and fluorescence quantum yield, respectively. Note that in the case of octahedral clusters fluorescence is not common, while phosphorescence is the predominant way of radiative energy dissipation.

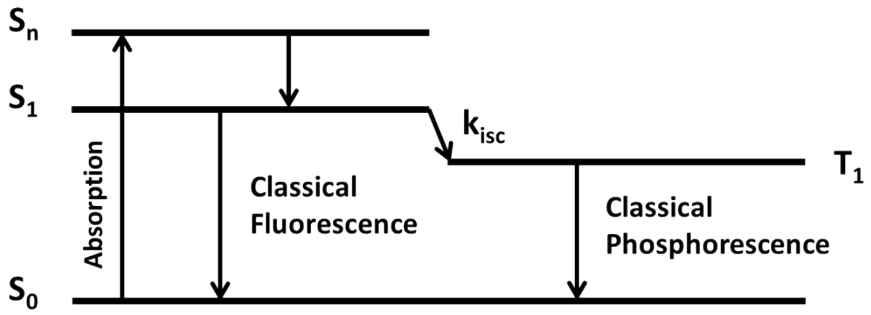

Figure S10. General Jablonski diagram illustrating fluorescence and phosphorescence processes.

The emission intensity is determined by a luminophore's excitation efficiency and its quantum yield. Excitation efficiency is influenced by the nature of phosphor, namely by its optical density. Quantum yield (Φ_0) is determined by the radiative (Γ) and non-radiative decay rates (k_{nr}). In the case of photosensitisers such as cluster complexes, quantum yield is also affected by the rate of singlet oxygen production, $k_q[^3O_2]$, where k_q is the rate of the triplet excited state quenching by molecular oxygen and $[^3O_2]$ is the concentration of oxygen. In summary quantum yield of octahedral cluster's phosphorescence can be expressed as the following equation:

$$\Phi_0 = \frac{\Gamma}{\Gamma + k_{nr} + k_q \times [^3O_2]} \quad (1)$$

In the presence of plasmonic particles due to the optimal match of the clusters' emission spectrum with the SPR band of GNSs, in the first instance emitted photons from the clusters upon excitation are partially absorbed by the particle to cause the surface plasmon resonance, which results in the local electric field enhancement. As described in earlier studies,[7, 8] SPR and electric field enhances emission intensity and excitation efficiency, correspondingly. Generally, luminescence of the clusters in the presence of the plasmonic nanostructure can be described by the following equation:

$$\frac{\gamma_{em}}{\gamma_{em}^0} = \frac{\gamma_{exc}}{\gamma_{exc}^0} \times \frac{\Phi}{\Phi_0} \quad (2)$$

where γ_{em} and γ^0_{em} are the luminescence rates of a single molecule with and without metal nanostructures, respectively. γ_{exc} and γ^0_{exc} are the excitation rates with and without metal nanostructures, respectively. γ_{exc} is proportional to $|E \cdot p|$, in which E is the local electric field and p is the transition dipole moment. Φ and Φ_0 are the quantum yields with and without metal nanostructures, respectively. Φ can be further expressed as:

$$\Phi = \frac{\Gamma + \Gamma_m}{\Gamma + \Gamma_m + k_m + k_{nr} + k_{q[O_2]}} \quad (3)$$

where Γ_m and k_m are additional radiative and nonradiative decay rates of the excited state, respectively, in the presence of metal nanostructures.

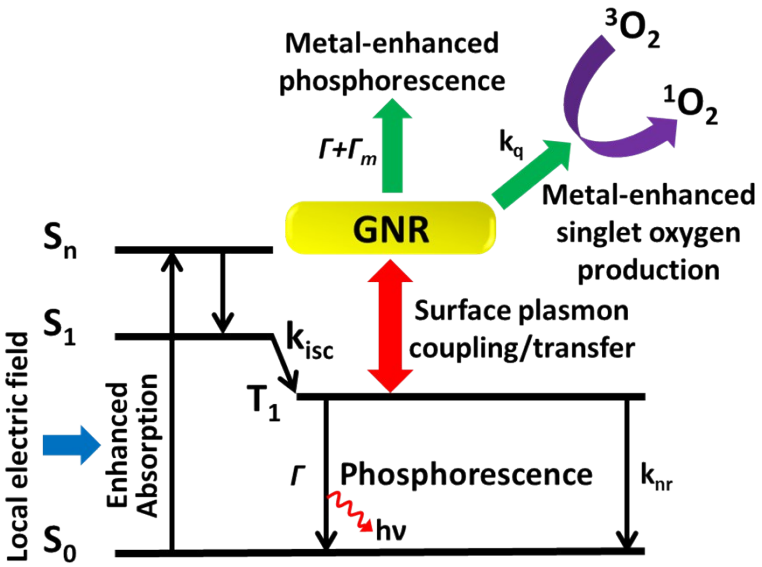

Figure S11. Modified Jablonski diagram illustrating phosphorescence and singlet oxygen generation processes in the presence of plasmonic particle.

In summary, the luminescence of octahedral clusters can be affected by plasmonic nanoparticles in the three following ways (Figure S11): (i) local electric field on the surface of metal nanostructures enhances excitation rate (γ_{exc}) and leads to further enhancement of excitation efficiency (equation 2). (ii) surface plasmon-coupled emission from coupling of the emission with the plasmons of metal nanostructures causes increase of radiative decay rate (Γ_m), which leads to increased quantum yields (equation 3); (iii) non-radiative energy transfer from the phosphors to metal nanostructures leads to increased non-radiative decay rate (k_m) which results in fluorescence quenching (equation 3).[7, 8] These three effects decrease with the increase of the distance between phosphor and metal nanostructure. According to earlier studies, the non-radiative energy transfer dominates at the metal surface and decreases proportionally to d^{-3} (where d is distance between particle surface and luminophore), while the local field effect decays exponentially from the surface. Thus, intensity of emission is proportional to $\exp(-d)/d^{-3}$. Therefore, there is an optimal cluster-to-gold distance whereupon emission intensity is maximal.
In regards to singlet oxygen production, literature suggests that enhancement is possible due to the enhanced triplet excited state yield of a sensitiser (Figure S11).[9, 10] As was mentioned above, local electric field enhances excitation efficiency, which results in higher amount of triplet states, which directly impact the efficiency of singlet oxygen generation.[11]

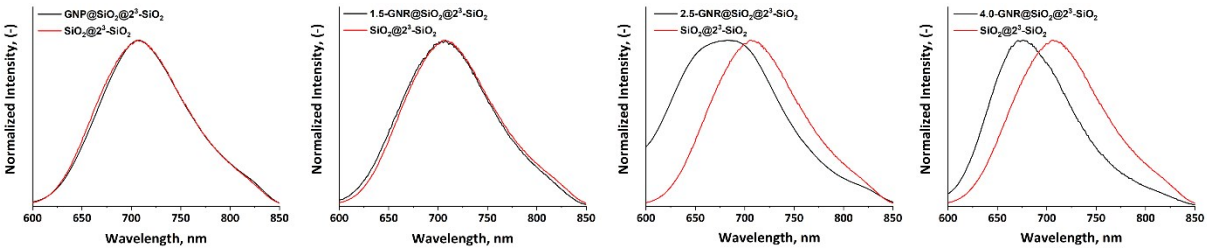

Figure S12. Comparison of normalised emission spectra profiles of SiO_2@**2**-SiO_2 (red) with GNP@SiO_2@**2**-SiO_2 or AR-GNR@SiO_2@**2**-SiO_2 with different AR (black). λ_{ex} = 365 nm.

Singlet oxygen generation study

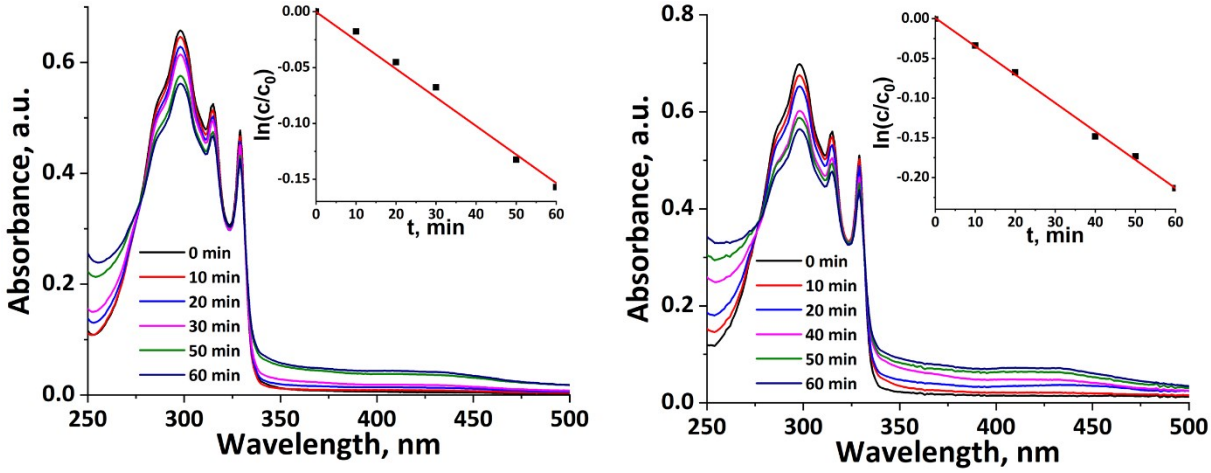

Figure S13. UV-vis spectra of 1,5-dihydroxynaphthalene (DHN) transformation in the presence of SiO_2@**n**-SiO_2 particles (for all samples C_{Mo} = 36 μg mL^{-1}) under UV irradiation (λ = 365 nm), n = **1** (*left*) and **2** (*right*). The inserts are linear approximation of ln(C/C_0) *vs* time.

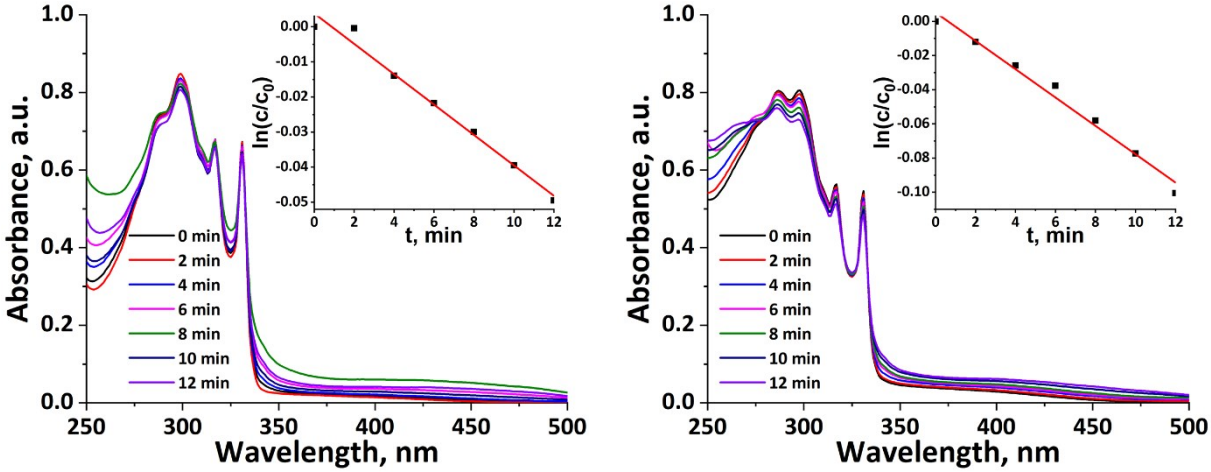

Figure S14. UV-vis spectra of 1,5-dihydroxynaphthalene (DHN) transformation in the presence of GNP@SiO_2@**n**-SiO_2 particles (for all samples C_{Mo} = 36 μg mL^{-1}) under UV irradiation (λ = 365 nm), n = **1** (*left*) and **2** (*right*). The inserts are a linear approximation of ln(C/C_0) *vs* time.

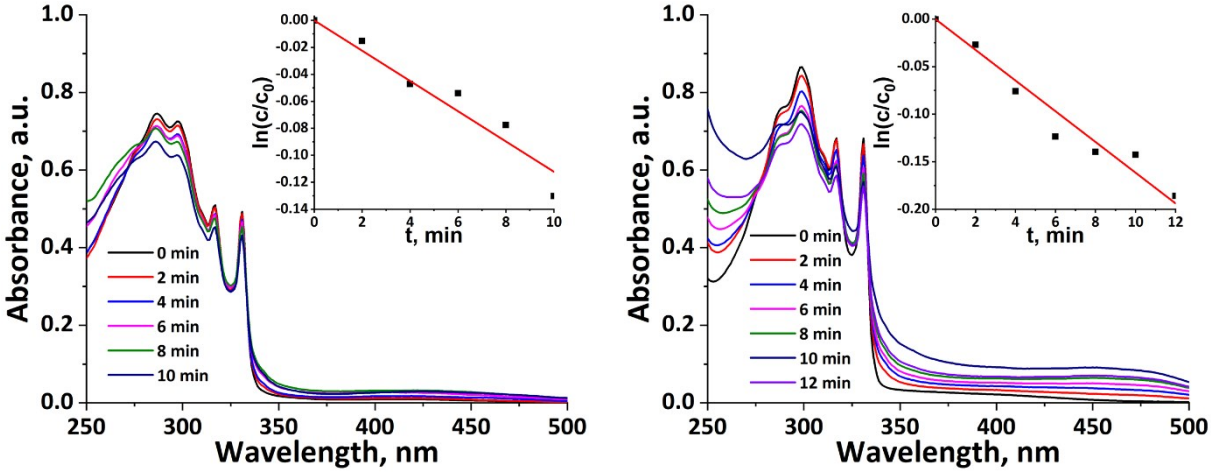

Figure S15. UV-vis spectra of 1,5-dihydroxynaphthalene (DHN) transformation in the presence of 1.5-GNR@SiO_2@**n**-SiO_2 particles (for all samples C_{Mo} = 36 μg mL^{-1}) under UV irradiation (λ = 365 nm), n = **1** (*left*) and **2** (*right*). The inserts are a linear approximation of $\ln(C/C_0)$ *vs* time.

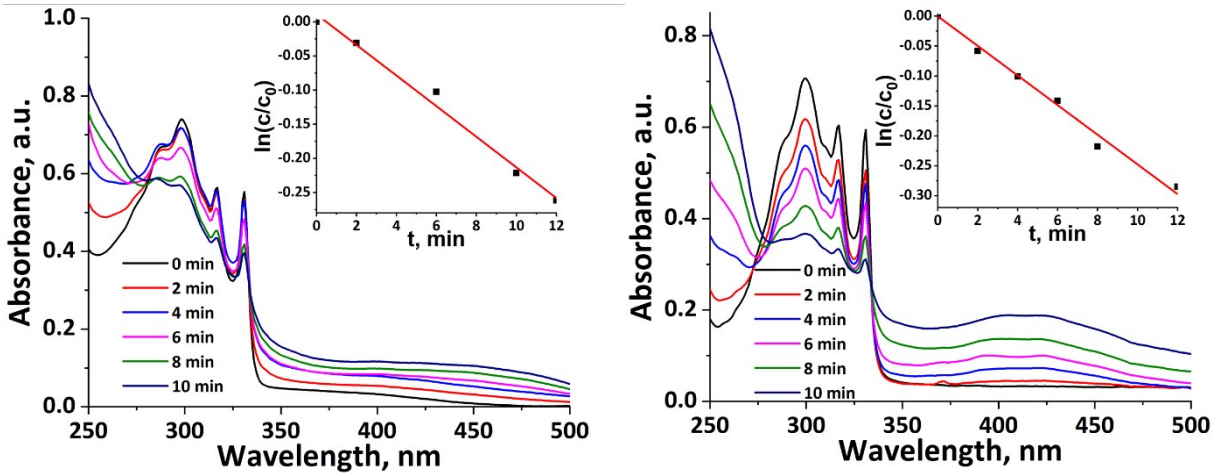

Figure S16. UV-vis spectra of 1,5-dihydroxynaphthalene (DHN) transformation in the presence of 2.5-GNR@SiO_2@**n**-SiO_2 particles (for all samples C_{Mo} = 36 μg mL^{-1}) under UV irradiation (λ = 365 nm), n = **1** (*left*) and **2** (*right*). The inserts are a linear approximation of $\ln(C/C_0)$ *vs* time.

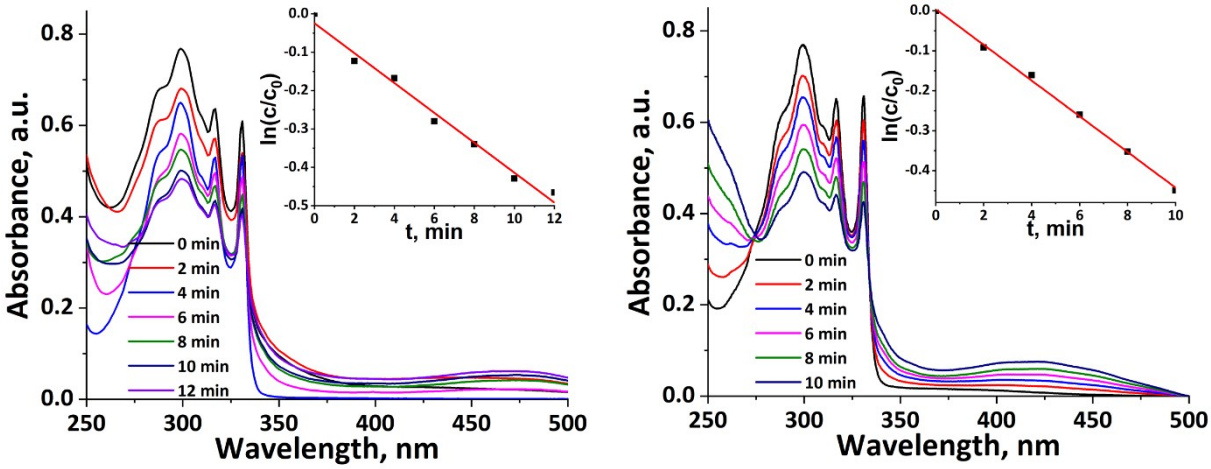

Figure S17. UV-vis spectra of 1,5-dihydroxynaphthalene (DHN) transformation in the presence of 4.0-GNR@SiO_2@**n**-SiO_2 particles (for all samples C_{Mo} = 36 μg mL^{-1}) under UV irradiation (λ = 365 nm), n = **1** (*left*) and **2** (*right*). The inserts are a linear approximation of $\ln(C/C_0)$ *vs* time.

Table S5. Known data on emission and singlet oxygen production enhancement factors by silica-covered GNPs/GNRs.

Description of the nanoparticles	Emission EF	Singlet oxygen production EF	References
GNP@SiO_2@FITC d (GNP) = 70 nm; silica shell thickness = 12 nm	2.03	-	[12]
GNR@mSiO_2–DOX/HP/R6G GNR length = 54.0 ± 5.0 nm; GNR width = 13.0 ± 1.5 nm; AR = 4.2 ± 0.5; mesoporous silica shell thickness = 20.2 ± 2.5 nm	1.2 R6G 2.9 DOX 3.8 HP	-	[13]
GNP@SiO_2−RB d (GNP) = 100 ± 7 nm; silica shell thickness = 10 nm	5.5	-	[14]
GNP@SiO_2−RB d (GNP) = 121.3 ± 3.8 nm; silica shell thickness = 9.9 ± 0.6 nm	-	6.1	[15]
GNR/mSiO_2-HP GNR length = 44 ± 8 nm; GNR width = 11 ± 2 nm; AR = 4; mesoporous silica shell thickness = 30 ± 7 nm	-	1.2	[16]
GNR-Si-ZnPc GNR length = 51 ± 2 nm; GNR width = 15 ± 3 nm; AR = 3.4; silica shell thickness = 15 ± 2 nm	-	1.3	[17]
GNR@SiO_2-AlC_4Pc GNR length = 46.8 ± 3.2 nm; GNR width = 19.4 ± 1.1 nm; AR = 2.4; silica shell thickness = 10.6 nm	7	2.1	[18]
GNP@SiO_2@**n**-SiO_2 d (GNP) = 107 ± 7 nm; silica shell thickness = 21 ± 2 nm	2.2	1.5 (n = **1**); 2.4 (n = **2**)	[5]
1.5-GNR@SiO_2@**n**-SiO_2	2.5 (n = **1**); 3.2 (n = **2**)	4.0 (n = **1**); 4.1 (n = **2**)	This work
2.5-GNR@SiO_2@**n**-SiO_2	3.6 (n = **1**); 3.8 (n = **2**)	7.5 (n = **1**); 6.7 (n = **2**)	This work
4.0-GNR@SiO_2@**n**-SiO_2	6.7	13 (n = **1**); 12 (n = **2**)	This work

References

1. O. A. Efremova, Y. A. Vorotnikov, K. A. Brylev, N. A. Vorotnikova, I. N. Novozhilov, N. V. Kuratieva, M. V. Edeleva, D. M. Benoit, N. Kitamura, Y. V. Mironov, M. A. Shestopalov and A. J. Sutherland, *Dalton Trans.*, 2016, **45**, 15427-15435.
2. O. A. Efremova, M. A. Shestopalov, N. A. Chirtsova, A. I. Smolentsev, Y. V. Mironov, N. Kitamura, K. A. Brylev and A. J. Sutherland, *Dalton Trans.*, 2014, **43**, 6021-6025.
3. B. Nikoobakht and M. A. El-Sayed, *Chem. Mater.*, 2003, **15**, 1957-1962.
4. A. P. Leonov, J. W. Zheng, J. D. Clogston, S. T. Stern, A. K. Patri and A. Wei, *Acs Nano*, 2008, **2**, 2481-2488.
5. E. D. Novikova, Y. A. Vorotnikov, N. A. Nikolaev, A. R. Tsygankova, M. A. Shestopalov and O. A. Efremova, *Chem. Eur. J.*, 2021, **27**, 2818-2825.
6. H. B. Lee, Y. M. Yoo and Y.-H. Han, *Scr. Mater.*, 2006, **55**, 1127-1129.
7. E. Fort and S. Gresillon, *J. Phys. D. Appl. Phys.*, 2008, **41**, Artn 013001.
8. J. R. Lakowicz, *Anal. Biochem.*, 2005, **337**, 171-194.
9. Y. X. Zhang, K. Aslan, M. J. R. Previte, S. N. Malyn and C. D. Geddes, *J. Phys. Chem. B*, 2006, **110**, 25108-25114.
10. Y. X. Zhang, K. Aslan, M. J. R. Previte and C. D. Geddes, *J. Fluoresc.*, 2007, **17**, 345-349.
11. J. C. Ostrowski, A. Mikhailovsky, D. A. Bussian, M. A. Summers, S. K. Buratto and G. C. Bazan, *Adv. Funct. Mater.*, 2006, **16**, 1221-1227.
12. Y.-T. Liu, X.-F. Luo, Y.-Y. Lee and I. C. Chen, *Dyes Pigm.*, 2021, **190**, ARTN 109263.
13. X. J. Tian, J. Guo, Y. Tian, H. Y. Tang and W. L. Yang, *RSC Adv.*, 2014, **4**, 9343-9348.
14. H. H. Lin and I. C. Chen, *J. Phys. Chem. C*, 2015, **119**, 26663-26671.
15. N. Macia, V. Kabanov and B. Heyne, *J. Phys. Chem. C*, 2020, **124**, 3768-3777.
16. T. T. Zhao, H. Wu, S. Q. Yao, Q. H. Xu and G. Q. Xu, *Langmuir*, 2010, **26**, 14937-14942.
17. H. P. Tham, H. Z. Chen, Y. H. Tan, Q. Y. Qu, S. Sreejith, L. Z. Zhao, S. S. Venkatraman and Y. L. Zhao, *Chem. Commun.*, 2016, **52**, 8854-8857.
18. X. B. Ke, D. Wang, C. Q. Chen, A. Q. Yang, Y. Han, L. Ren, D. H. Li and H. J. Wang, *Nanoscale Res. Lett.*, 2014, **9**, ARTN 666.